

Clustering of emission line galaxies with IllustrisTNG – II. cosmology challenge with anisotropic correlation functions and ELG-halo connections

Ken Osato^{1,2,3,4*} and Teppei Okumura^{5,4}

¹Center for Frontier Science, Chiba University, 1-33 Yayoi-cho, Inage-ku, Chiba 263-8522, Japan

²Department of Physics, Graduate School of Science, Chiba University, 1-33 Yayoi-cho, Inage-ku, Chiba 263-8522, Japan

³RIKEN Center for Advanced Intelligence Project, 1-4-1 Nihonbashi, Chuo-ku, Tokyo 103-0027, Japan

⁴Kavli Institute for the Physics and Mathematics of the Universe, The University of Tokyo Institutes for Advanced Study,

5-1-5 Kashiwanoha, Kashiwa-shi, Chiba, 277-8583, Japan

⁵Academia Sinica Institute of Astronomy and Astrophysics, No. 1, Section 4, Roosevelt Road, Taipei 10617, Taiwan

Accepted XXX. Received YYY; in original form ZZZ

ABSTRACT

Emission line galaxies (ELGs) are the primary tracers of the large-scale structures of the Universe in ongoing Stage-IV cosmological spectroscopic surveys, which aim to measure the clustering statistics at higher redshifts $z \simeq 1.5\text{--}2$ with unprecedented precision. In this study, we construct realistic mock ELG samples with IllustrisTNG hydrodynamical simulations and stellar population synthesis framework. In order to validate the modelling of clustering, we measure the anisotropic correlation functions of mock ELGs and infer the linear growth rate, which is one of key cosmological parameters in galaxy clustering. As a control sample, we construct the mass-limited subhalo samples with the same number density as ELGs. The isotropic correlation functions in real space for both samples do not differ significantly. However, the quadrupole moment of the anisotropic correlation function, which is sensitive to the velocity of galaxies, is suppressed for ELGs, potentially due to the infalling motion of ELGs towards the centre of the hosting halos. The smaller amplitude leads to the underestimation of the linear growth rate and implies the velocity bias between ELGs and dark matter. When the analysis is limited to large scales ($\gtrsim 15 h^{-1} \text{ Mpc}$), the parameter bias vanishes. Next, we investigate the ELG-halo connection through the phase-space distribution of satellite ELGs within hosting halos and galactic conformity of star formation activity. The infalling motion is further confirmed by the phase-space distribution relative to the host halo, and this dynamics of ELGs challenges the assumption that the radial distribution of satellites follows that of dark matter.

Key words: large-scale structure of Universe – cosmology: theory – methods: numerical

1 INTRODUCTION

In the standard paradigm of cosmology, the density fluctuations are seeded in the early Universe as quantum fluctuations during the inflationary era, and a myriad of structures are hierarchically formed through gravitational instability (White & Rees 1978; White & Frenk 1991; Cole et al. 2000). The gravitational evolution is driven primarily by dark matter, and thus, the large-scale structure (LSS) of the Universe is one of the key probes into the nature of dark matter and gravity theory (for a review, see Weinberg et al. 2013). Furthermore, in the late-time Universe, the expansion of the space-time accelerates due to dark energy. To investigate the geometry of the Universe, the sound horizon of cosmic plasma, which is referred to as baryon acoustic oscillation (BAO) scale, has played an important role. BAO is the oscillatory feature imprinted in the matter distribution and serves as a cosmic standard ruler. Through the statistical measurement of the BAO scale, the physical nature of dark energy can be robustly addressed (Eisenstein et al. 2005; Aubourg et al. 2015).

The foremost challenge in observations of LSS is that dark matter is not visible from telescopes. Hence, in the real measurements of

the LSS, galaxies are widely used as tracers of the underlying matter distribution, which is the direct consequence of gravitational evolution from density perturbations. On large scales, the approximation that the galaxy number density contrast is linearly proportional to the matter density contrast holds well. On the other hand, the relationship between matter and galaxy, i.e., *galaxy-halo connection* (for a review, see Wechsler & Tinker 2018), becomes complex on small scales. In practice, halo occupation distribution (HOD; Berlind & Weinberg 2002; Kravtsov et al. 2004) is the most popular model to connect galaxies from host dark matter halos. HOD describes the probability distribution of the number of galaxies as a function of the mass of the halo. This approach is successful in reproducing the two-point correlation functions of galaxies down to non-linear scales (Zehavi et al. 2004). For example, Zheng et al. (2005) proposed a five-parameter HOD, and in Zheng et al. (2009), the HOD is applied to model the correlation function of luminous red galaxies (LRGs; Eisenstein et al. 2001) observed by Sloan Digital Sky Survey. LRGs are selected based on colours and magnitudes so that the selected galaxies are a homogenous population with similar stellar mass and their photometric redshift is accurately estimated with 4000 Å break (Padmanabhan et al. 2007). A similar idea is brought to the sample selection of CMASS and LOWZ samples (Anderson et al. 2012;

* E-mail: ken.osato@chiba-u.jp

Reid et al. 2016) in Baryon Oscillation Spectroscopic Survey (BOSS; Dawson et al. 2013). Since LRGs are massive and old systems, the number density field of LRGs is highly biased against the matter density field, and the internal motion is well virialised. Therefore, the HOD and resultant clustering of LRGs are less sensitive to galaxy formation physics.

On the other hand, the next generation of spectroscopic surveys, which are referred to as Stage-IV spectroscopic surveys, including Dark Energy Spectroscopic Instrument (DESI; DESI Collaboration 2022), *Euclid* (Euclid Collaboration 2025), Subaru Prime Focus Spectrograph (PFS; Takada et al. 2014), and Roman Space Telescope (Spergel et al. 2015; Akeson et al. 2019), will target a different galaxy population: emission line galaxies (ELGs). ELGs are blue and star-forming galaxies characterised by the bright line emission, such as $\text{H}\alpha$ ($\lambda 6564.62 \text{ \AA}$), $[\text{O II}]$ ($\lambda\lambda 3727.09 \text{ \AA}, 3729.88 \text{ \AA}$), and $[\text{O III}]$ ($\lambda 5008.24 \text{ \AA}$). These line emissions are produced from nebular gas irradiated by massive OB-type stars (Charlot & Longhetti 2001; Kewley et al. 2019). ELGs have been utilised to diagnose the cosmic star formation history since the line emission reflects the star formation activity on a short time scale up to ~ 10 Myr (Byler et al. 2018) corresponding to the lifetime of OB-type stars. The reason why ELGs are the main target in the future surveys is that these surveys will measure galaxy clustering at higher redshifts ($z \simeq 1.5\text{--}2$), where the star formation activity is at its peak (Madau & Dickinson 2014; Förster Schreiber & Wuyts 2020), i.e., *cosmic noon*. At this epoch, the expected number density of ELGs is high, and thus, an accurate measurement of clustering statistics is possible. In addition, bright line emission helps to determine the redshift accurately. However, clustering of ELGs is not well studied compared with LRGs and the nature of ELGs is expected to be quite different from that of LRGs. In contrast to LRGs, ELGs are likely to be hosted by less massive and younger halos and undergo infall towards the halo. Hence, clustering of ELGs is subject to velocity bias, environment effects, and assembly bias.

Recently, several pilot observations targeting ELGs at $z \simeq 1\text{--}2$ have been conducted: HiZELS (Geach et al. 2008; Sobral et al. 2012), FastSound (Tonegawa et al. 2015; Okada et al. 2016; Okumura et al. 2016), and narrow band observations with Subaru Hyper Suprime-Cam (Hayashi et al. 2018, 2020; Okumura et al. 2021; Ishikawa et al. 2025). Subsequently, large spectroscopic survey programmes covering wider areas, e.g., eBOSS (Tamone et al. 2020; Raichoor et al. 2021; de Mattia et al. 2021) and DESI (DESI Collaboration 2025b, 2024, 2025a,c), have measured clustering statistics of ELGs and constrained cosmological parameters with two-point correlations.

To elucidate ELG clustering and ELG-halo connection from these observations, empirical approaches such as HOD and subhalo abundance matching (SHAM) have been widely utilised. The observations of ELGs so far indicate that extensions beyond HOD are demanded to improve the accuracy of modelling ELG clustering, e.g., different functional forms to incorporate the infalling component (Geach et al. 2012; Gao et al. 2022), adding physical parameters beyond halo mass (Hearin et al. 2016; Hadzhiyska et al. 2023b,a), modifications to velocity distribution of satellite ELGs (Avila et al. 2020; Rocher et al. 2023), and constraining HOD parameters jointly with luminosity functions (Ishikawa et al. 2025). Similarly, SHAM needs to be modified so that the star-formation rate (SFR) is properly modelled (Favole et al. 2022; Ortega-Martinez et al. 2024, 2025), because the ELG sample is close to an SFR-limited sample rather than a stellar mass-limited sample, which standard SHAM deals with.

As observations of ELGs advance, there is also substantial progress in numerical and theoretical studies of ELG clustering with hydrodynamical simulations (Hadzhiyska et al. 2021; Yuan

et al. 2022, 2025) and semi-analytic simulations (Gonzalez-Perez et al. 2018; Orsi & Angulo 2018; Favole et al. 2020; Gonzalez-Perez et al. 2020). These simulations enable in-depth investigation of ELG-halo connection since various halo properties are directly accessible. Based on these simulations, it is found that a large fraction of ELGs lie in filamentary structures and undergo infall toward more massive halos, and ELGs are hosted by younger and less concentrated halos (Yuan et al. 2022), which is the signature of galaxy assembly bias.

To scrutinise cosmology with ELGs and the ELG-halo connection, we have constructed a high-fidelity ELG mock catalogue based on IllustrisTNG simulations (Nelson et al. 2019) coupled with stellar population synthesis (SPS) code PÉGASE3 (Fioc & Rocca-Volmerange 2019) in our previous work (Osato & Okumura 2023, hereafter, Paper I). In PÉGASE3, nebular line emissions are derived from the precomputed table by photo-ionization code CLOUDY (Ferland et al. 2017), which simulates synthesised spectra in the star-forming clouds. The scheme is useful to interpret various line emissions of star-forming galaxies (Gutkin et al. 2016). The nebular emissions are subject to dust extinction due to dust in birth clouds (Charlot & Fall 2000) in addition to inter-stellar medium (for a review, see Salim & Narayanan 2020). Since the dust formation and evolution is analytically modelled in PÉGASE3, the extinction effect is properly taken into account. We first construct a precomputed table of $\text{H}\alpha$ and $[\text{O II}]$ line emissions in the grids of metallicity and stellar age. Then, we assign emissions from each stellar particle by looking up the table, and sum all the contributions from member stellar particles in each simulated galaxy. The mock ELG samples show agreement with observed line luminosity functions. We have investigated HOD and projected correlation functions of mock ELGs in Paper I. Recently, Rapoport et al. (2025) presented an approach to simulate $\text{H}\alpha$ emission with hydrodynamical simulations based on a simple radiative transfer model, which is complementary to our approach utilising the SPS model.

In this work, we extend the analysis presented in Paper I to address cosmology with ELGs and the ELG-halo connection. First, we measure anisotropic correlation functions of ELGs in redshift space, which are primary statistics to constrain cosmological parameters and gravity models. Since ELGs entail dynamics within halos different from LRGs, i.e., infalling along filaments, that feature propagates to cosmological statistics. Hence, it is not clear whether the current modelling of cosmological statistics can infer unbiased cosmological parameters. Thus, since the cosmological parameters are given in simulations, we can conduct *cosmology challenge* analysis to confirm that the inferred cosmological parameters can be reproduced without bias. This analysis is critical to validate the theoretical template of ELG clustering. Next, we address ELG-halo connection with the mock ELG catalogues. Since properties of halos hosting ELGs are readily available in simulations, we closely investigate ELG-halo connection and identify the elements which incur the difference in cosmological statistics.

This paper is organised as follows. In Section 2, we outline how mock ELG catalogues are built from IllustrisTNG hydrodynamical simulations. In Section 3, theoretical modelling of anisotropic correlation functions is explained. We present the results of the cosmology challenge in Section 4 and ELG-halo connection in Section 5. We conclude in Section 6. In Appendix A, the theoretical modelling of galaxy power spectra in real space is described. In Appendix B, auxiliary analytic expressions for multipole expansion are presented. For cosmology challenge, the results with $[\text{O II}]$ ELG sample are discussed in the main text and the results with $\text{H}\alpha$ ELG sample are shown in Appendix C. Throughout this paper, we assume the flat Λ cold dark matter Universe and following cosmological pa-

rameters adopted in IllustrisTNG simulations: the baryon density $\Omega_b = 0.0486$, the matter density $\Omega_m = 0.3089$, the cosmological constant density $\Omega_\Lambda = 1 - \Omega_m = 0.6911$, the scaled Hubble parameter $h = 0.6774$, the tilt of the primordial perturbations $n_s = 0.9667$, and the amplitude of matter fluctuation at $8 h^{-1} \text{ Mpc}$ $\sigma_8 = 0.8159$.

2 CONSTRUCTION OF MOCK ELG SAMPLES

2.1 Modelling emission lines in hydrodynamical simulations

First, we describe the scheme to compute emission line luminosities for each simulated galaxy in hydrodynamical simulations. For more details, refer to Section 2 of [Paper I](#).

To construct mock ELG catalogues, we employ IllustrisTNG hydrodynamical simulations ([Nelson et al. 2018](#); [Pillepich et al. 2018b](#); [Springel et al. 2018](#); [Naiman et al. 2018](#); [Marinacci et al. 2018](#); [Nelson et al. 2019](#)). The simulations are run with the moving mesh code AREPO ([Springel 2010](#)) and various galaxy formation processes, such as star formation and feedback effects due to supernovae and active galactic nuclei are implemented as a subgrid model ([Weinberger et al. 2017](#); [Pillepich et al. 2018a](#)). The subgrid model parameters are calibrated so that the observations of galactic properties, e.g., stellar mass functions, can be reproduced. Among IllustrisTNG simulations with different box sizes and resolutions, TNG300-1 simulation is utilised as the fiducial one. The simulation volume is $(205 h^{-1} \text{ Mpc})^3$ and the number of dark matter particles and gas cells is 2500^3 , which corresponds to the mass resolution of $m_{\text{DM}} = 5.9 \times 10^7 h^{-1} M_\odot$ and $m_{\text{gas}} = 1.4 \times 10^6 h^{-1} M_\odot$ for dark matter and gas, respectively. Halos and their substructures, i.e., subhalos, are identified with SubFind algorithm ([Springel et al. 2001](#)). As terminology, a simulated *galaxy* corresponds to a *subhalo* in simulations.

Next, we compute emission line luminosities by post-processing simulation outputs. The stellar component of a simulated galaxy is expressed as an assembly of stellar particles, each of which records the formation time, metallicity, and the mass at the formation time. For each stellar particle, line luminosity is calculated with the SPS code PÉGASE3 ([Fioc & Rocca-Volmerange 2019](#)), where nebular emission is derived from the precomputed results of CLOUDY ([Ferland et al. 2017](#)). Thus, we construct a table of line emissions ($\text{H}\alpha$ and $[\text{O}\,\text{II}]$) with respect to the stellar age and metallicity. For the total line luminosity, we sum the contribution from each stellar particle, which is bilinearly interpolated for the stellar age and metallicity from the table, weighted with the mass. Note that nebular line emission is subject to dust extinction and the extinction must be incorporated. Otherwise, the number density of ELGs is highly overestimated. PÉGASE3 adopts a phenomenological dust evolution model (see Section 3.2 of [Fioc & Rocca-Volmerange 2019](#)), where the dust mass is proportional to the mass of inter-stellar medium. Though the model is calibrated with Milky Way observations, the resultant line luminosity functions match well with observations at high redshifts $z = 1\text{--}2$ (see Figure 2 of [Paper I](#)).

2.2 Emission line galaxy and mass-limited subhalo control samples

First, we construct two target ELG samples selected with $\text{H}\alpha$ and $[\text{O}\,\text{II}]$ line luminosities from the parent catalogue described in the previous section. These are strong line emissions from star-forming nebulae and are used to construct galaxy catalogues in the Stage-IV survey: $\text{H}\alpha$ for *Euclid*, and $[\text{O}\,\text{II}]$ for DESI and PFS. Hereafter, only the catalogue at the redshift $z = 1.5$ is considered, which is

a typical redshift for Stage-IV spectroscopic surveys. In this work, galaxies with the line luminosity higher than $2 \times 10^{42} \text{ erg s}^{-1}$ or $1 \times 10^{42} \text{ erg s}^{-1}$ are defined as $\text{H}\alpha$ or $[\text{O}\,\text{II}]$ ELGs, respectively. The corresponding flux limit is $6.71 \times 10^{-17} \text{ erg s}^{-1} \text{ cm}^{-2}$ for $\text{H}\alpha$ ELGs and $1.34 \times 10^{-16} \text{ erg s}^{-1} \text{ cm}^{-2}$ for $[\text{O}\,\text{II}]$ ELGs. These flux limits are chosen to mimic the expected flux limit of *Euclid* $\text{H}\alpha$ and PFS $[\text{O}\,\text{II}]$ ELGs. The resultant $\text{H}\alpha$ and $[\text{O}\,\text{II}]$ ELG samples consist of 6,864 and 11,001 galaxies, and the comoving number density is $7.97 \times 10^{-4} (h^{-1} \text{ Mpc})^{-3}$ and $1.28 \times 10^{-3} (h^{-1} \text{ Mpc})^{-3}$, respectively. To highlight the difference from ELGs, we also construct control samples for $\text{H}\alpha$ and $[\text{O}\,\text{II}]$ ELGs, which are the subhalo mass limited samples with the same number densities. The mass limit of the control samples for $\text{H}\alpha$ and $[\text{O}\,\text{II}]$ ELGs is $2.09 \times 10^{12} h^{-1} M_\odot$ and $1.51 \times 10^{12} h^{-1} M_\odot$, respectively. These samples exhibit the similar galaxy bias to the corresponding ELG samples but are expected to indicate the different nature in velocity and statistics in redshift space.

3 THEORETICAL MODEL FOR ANISOTROPIC CORRELATION FUNCTIONS

Here, we describe the theoretical model of the anisotropic correlation functions. In spectroscopic surveys, the line-of-sight (LoS) positions of galaxies are estimated from the redshift. The redshift estimation is distorted by the peculiar velocity of the galaxy, which is referred to as redshift space distortion (RSD). This effect induces the anisotropy in clustering statistics and needs to be incorporated in the theoretical modelling of clustering statistics for unbiased estimation of cosmological parameters.

First, we begin with galaxy power spectra in redshift space. We employ the extended Taruya–Nishimichi–Saito (eTNS) model [Taruya et al. \(2010, 2013\)](#). The galaxy power spectrum in this model is given as

$$P_{\text{gg}}(k, \mu) = D_{\text{FoG}}(k\mu\sigma_v) [P_{\delta_g \delta_g}(k) + 2f\mu^2 P_{\delta_g \theta_g}(k) + f^2\mu^4 P_{\theta_g \theta_g}(k) + b_1^3 A(k, \mu, \beta) + b_1^4 B(k, \mu, \beta)], \quad (1)$$

where D_{FoG} is the Finger-of-God (FoG) damping function, δ_g is the density contrast of galaxies, θ_g is the velocity divergence field of galaxies, $P_{\delta_g \delta_g}(k)$, $P_{\delta_g \theta_g}(k)$, and $P_{\theta_g \theta_g}(k)$ are the density-density auto-, density-velocity cross-, and velocity-velocity auto-power spectra in real space, respectively, and b_1 is the linear bias parameter. Here, μ is the cosine of the angle between the wave vector \mathbf{k} and the LoS direction, and the velocity divergence of galaxies θ_g is expressed as $\theta_g = \nabla \cdot \mathbf{v}_g / (aH)$, where \mathbf{v}_g is the peculiar velocity of galaxies, a is the scale factor, and H is the Hubble parameter. The second and third terms in Eq. (1) correspond to the Kaiser effect ([Kaiser 1987](#)), which enhances the clustering signal at the large scale due to coherent infall towards the potential well. The linear growth rate $f = d \log D_+ / d \log a$, where D_+ is the linear growth factor, regulates the enhancement and is sensitive to the underlying gravity theory. In contrast to the Kaiser effect, the FoG effect refers to smearing at small scales due to random motions of galaxies ([Jackson 1972](#)), and the damping feature is well explained by the phenomenological model to suppress the amplitude of the power spectrum. We adopt the Lorentzian form of FoG damping function $D_{\text{FoG}}(x) = (1 + x^2/2)^{-2}$. The last terms, $A(k, \mu, \beta)$ and $B(k, \mu, \beta)$ with $\beta = f/b_1$, are non-linear coupling correction terms presented in [Taruya et al. \(2010\)](#) and the details will be described later. All the expressions of power spectra and correction terms depend on the redshift z , but we omit its dependence hereafter for notational simplicity.

For modelling of real-space galaxy power spectra, $P_{\delta_g \delta_g}(k)$,

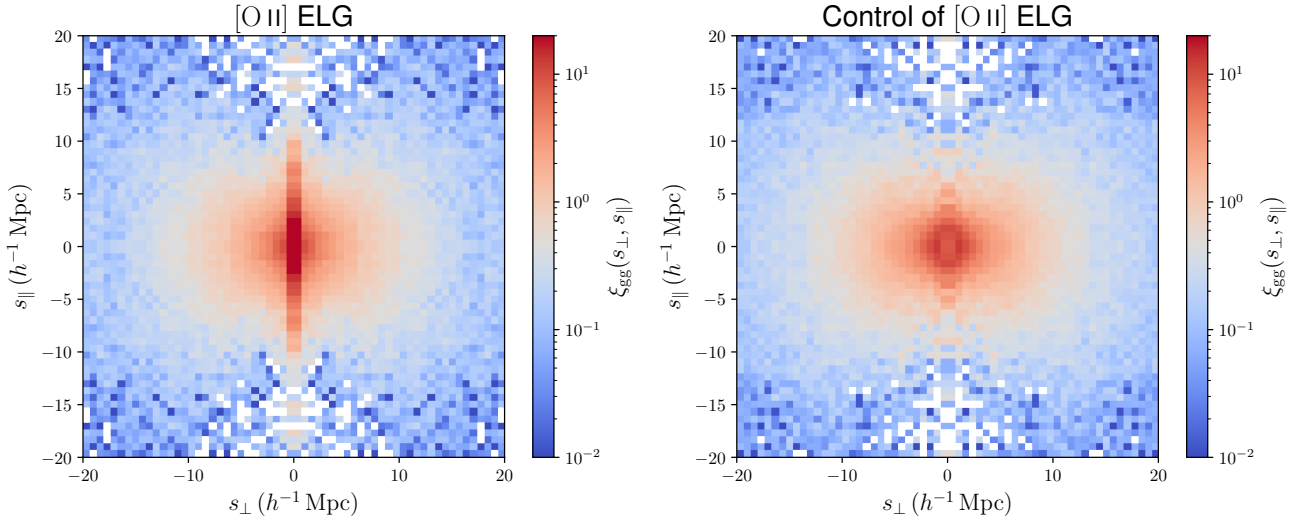


Figure 1. The 2D anisotropic correlation functions of [O II] ELGs and the corresponding control sample. The white pixels correspond to the no pair in the measurement.

$P_{\delta_g \theta_g}(k)$, and $P_{\theta_g \theta_g}(k)$, we adopt the model presented in McDonald & Roy (2009) based on galaxy bias expansion. Since the model requires the non-linear power spectra of matter density and velocity, the non-linear matter power spectrum is computed with **HMCODE-2020** (Mead et al. 2021), and for velocity spectrum, the fitting formula by Bel et al. (2019) is employed. The details of the model are presented in Appendix A. One of the key assumptions in this model is no velocity bias for galaxies, i.e., $\theta_g = \theta$, where θ is the velocity divergence field of matter. This relation may not hold for ELGs and will be addressed through estimation of the linear growth rate because the break of this relation appears as the bias in the inferred linear growth rate.

Finally, let us consider the non-linear coupling terms $A(k, \mu, \beta)$ and $B(k, \mu, \beta)$ based on perturbation theory (Taruya et al. 2010). The terms are computed at the 1-loop order with regularized perturbation theory (Taruya et al. 2012, 2013). In the presence of the linear bias, the coupling terms scale as

$$A(k, \mu, f) \rightarrow b^3 A(k, \mu, \beta), \quad (2)$$

$$B(k, \mu, f) \rightarrow b_1^4 B(k, \mu, \beta). \quad (3)$$

In total, there are four bias parameters ($b_1, b_2, b_{s2}, b_{3nl}$) in galaxy power spectrum. However, these parameters are tightly degenerate with cosmological parameters, especially for the limited survey volume. In order to obtain converged results, we adopt the local Lagrangian relation for b_{s2} and b_{3nl} (Baldauf et al. 2012; Chan et al. 2012; Sheth et al. 2013; Saito et al. 2014; Mirbabayi et al. 2015):

$$b_{s2} = -\frac{4}{7}(b_1 - 1), \quad (4)$$

$$b_{3nl} = \frac{32}{315}(b_1 - 1). \quad (5)$$

For the second order bias b_2 , we adopt the fitting formula presented in Lazeyras et al. (2016):

$$b_2 = 0.412 - 2.143b_1 + 0.929b_1^2 + 0.008b_1^3. \quad (6)$$

The relation is calibrated with halos but holds well for galaxies selected with star formation rate in hydrodynamical simulations (Barreira et al. 2021). In summary, there is only one free bias parameter b_1 and other bias parameters are derived from Eqs. (4), (5), and (6).

The multipole expansion of the galaxy power spectrum is given as

$$P_\ell(k) = \frac{2\ell + 1}{2} \int_{-1}^{+1} d\mu P_{gg}(k, \mu) L_\ell(\mu), \quad (7)$$

where $L_\ell(\mu)$ is the ℓ -th order Legendre polynomial. The dependence on the directional cosine μ in the eTNS 2-loop model except the FoG damping function is the polynomial at even degrees up to the octic. The integration can be done analytically, and the conversion formulae are presented in Appendix B. Then, the multipoles of the anisotropic correlation functions are obtained through Hankel transformation:

$$\xi_\ell(s) = i^\ell \int \frac{k^2 dk}{2\pi^2} P_\ell(k) j_\ell(ks), \quad (8)$$

where $j_\ell(x)$ is the ℓ -th order spherical Bessel function. We utilise FFTLog (Hamilton 2000) algorithm to compute Hankel transformation efficiently. Due to the symmetry in directions perpendicular to the LoS direction, the moments at odd orders vanish. The moments at higher orders are expected to be noisy, and thus, we focus only on the monopole ($\ell = 0$) and quadrupole ($\ell = 2$) moments for the subsequent analysis.

There is one caveat about Alcock–Paczynski (AP) effect (Alcock & Paczynski 1979). The largest scale in the correlation function is limited by the box size of simulations, i.e., $205 h^{-1}$ Mpc, and thus, the BAO scale cannot accurately be probed in the analysis. Hence, we do not include the AP effect in the theoretical modelling of anisotropic correlation functions.

4 COSMOLOGY CHALLENGE WITH THE ANISOTROPIC CORRELATION FUNCTIONS

4.1 Mock measurements of the correlation functions

Here, we present the scheme to measure the anisotropic correlation functions from the ELG catalogues. In this Section, we focus on the [O II] ELG sample and the corresponding mass-limited control sample. The results for H α ELG sample and the control sample are similar to [O II] ELG sample, and the selected key results are presented in Appendix C. Since the random pair count is analytically

computed under the periodic boundary condition, we employ the natural estimator of the correlation function (Peebles & Hauser 1974):

$$\hat{\xi}_{gg}(s_{\perp}, s_{\parallel}) = \frac{DD}{RR} - 1, \quad (9)$$

where s_{\perp} (s_{\parallel}) is the separation distance of the pair perpendicular (parallel) to the LoS direction in the redshift space, DD and RR is the pair counts of ELGs and randoms normalised by the total pair counts, respectively. The perpendicular and parallel separation is binned linearly in the range of $[0, 20] h^{-1}$ Mpc with 20 bins. The pair counts are computed with neighbour search algorithm using R-tree. In the measurements from simulations with the periodic boundary condition, the random pair counts are given as

$$RR = \frac{\Delta V}{V_{\text{sim}}}, \quad (10)$$

where $V_{\text{sim}} = (205 h^{-1} \text{ Mpc})^3$ is the simulation box volume, and ΔV is the volume occupied in the bin range.

In Figure 1, the measured 2D anisotropic correlation functions of [O II] ELGs and corresponding mass-limited control samples are shown. On large scales, the structure of correlation functions is quite similar between ELG and control samples. However, on small scales, the FoG effect appears differently due to the different dynamics within halos. We will address this feature in more details later.

Next, the estimator of the multipole moment of anisotropic correlation function (Valageas & Clerc 2012) is given as

$$\hat{\xi}_{\ell}(s) = \frac{2\ell + 1}{RR} \sum_{dd} L_{\ell}(\mu_{dd}) - \delta_{\ell 0}, \quad (11)$$

where s is the 3D separation distance in the redshift space, the summation is performed for all pairs of ELGs, μ_{dd} is the directional cosine with respect to the LoS direction, and δ_{ij} is the Kronecker delta. The separation is binned linearly in the range of $[5, 50] h^{-1}$ Mpc with 30 bins. For reference, the isotropic correlation function $\xi_{gg}(r)$ is also computed in the same manner, where the separation r is measured in real space, i.e., without RSD.

The covariance matrix of the multipole moments of the anisotropic correlation functions is estimated with bootstrapping method (e.g., Norberg et al. 2009; Pu et al. 2025). The bootstrap samples are constructed by resampling ELGs with duplications until the sample contains the same number of ELGs as the parent catalogue. Then, we repeat this procedure and $N_{\text{BS}} = 1120$ bootstrap samples. The covariance matrix is estimated as

$$\text{Cov}(\ell_a, s_i; \ell_b, s_j) = \frac{1}{N_{\text{BS}} - 1} \sum_{r=1}^{N_{\text{BS}}} \left(\xi_{\ell_a}^{(r)}(s_i) - \bar{\xi}_{\ell_a}(s_i) \right) \times \left(\xi_{\ell_b}^{(r)}(s_j) - \bar{\xi}_{\ell_b}(s_j) \right), \quad (12)$$

$$\bar{\xi}_{\ell_a}(s_i) = \frac{1}{N_{\text{BS}}} \sum_{r=1}^{N_{\text{BS}}} \xi_{\ell_a}^{(r)}(s_i). \quad (13)$$

The label a and b denotes the multipole order: monopole ($\ell = 0$) and quadrupole ($\ell = 2$) and the index i and j represent the bin of the separation distance. The covariance of the isotropic correlation functions is estimated in the same manner.

Figures 2 and 3 present the isotropic correlation functions and monopole and quadrupole moments of anisotropic correlation functions for [O II] ELGs and control samples, respectively. The amplitude of isotropic correlation functions of ELGs and control samples is similar since the control sample is constructed so that the number density is the same as the ELG samples, and thus, the sample exhibits

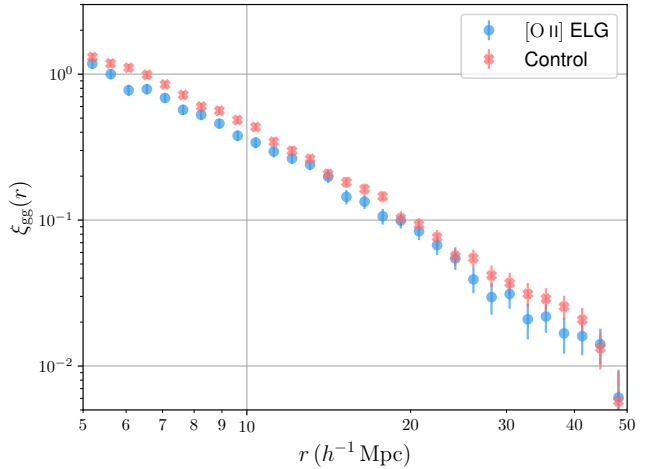


Figure 2. The isotropic correlation functions of [O II] ELGs and the corresponding control sample.

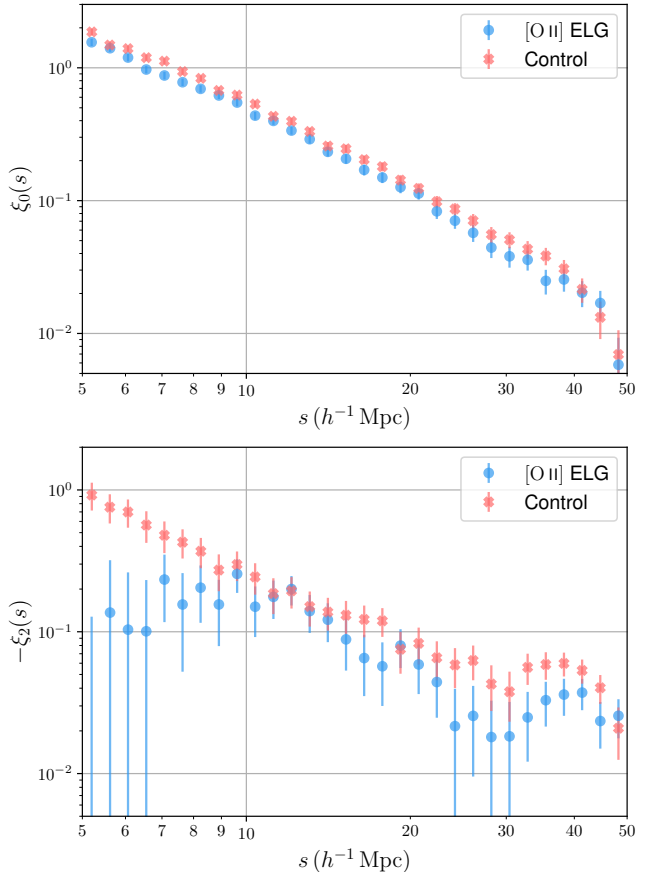


Figure 3. The monopole and quadrupole moments of correlation functions of [O II] ELGs and the corresponding control sample.

a similar galaxy bias. In contrast, the quadrupole moment shows a significant difference. The small-scale amplitude of the ELG sample is suppressed, and the overall amplitude is smaller than that of the control sample. This feature suggests that the velocity of ELGs, i.e., dynamics within halos, differs from that of the control sample.

4.2 Cosmological parameter inference

The primary objective of this work is to quantify the possible bias in cosmological parameters, especially the linear growth rate f , inferred from the anisotropic correlation functions of ELGs. As seen in the previous section, the dynamics of ELGs within halos can lower the amplitude of the quadrupole moment, which can be translated to an underestimation of the linear growth rate. Here, we describe the parameter inference from the mock measurements of anisotropic correlation functions.

In this analysis, the parameter space consists of the linear growth rate f , the linear bias parameter b_1 , and the velocity dispersion σ_v in the FoG damping function. The other cosmological parameters are fixed to the fiducial values (see Section 2). We assume that the likelihood takes the multivariate Gaussian form:

$$\log L(\boldsymbol{\theta}) = -\frac{1}{2} \sum_{a,b,i,j} (\hat{\xi}_{\ell_a}(s_i) - \xi_{\ell_a}(s_i; \boldsymbol{\theta})) \text{Cov}^{-1}(\ell_a, s_i; \ell_b, s_j) \times (\hat{\xi}_{\ell_b}(s_j) - \xi_{\ell_b}(s_j; \boldsymbol{\theta})) + \text{const.}, \quad (14)$$

where $\boldsymbol{\theta} = (f, b_1, \sigma_v)$ is the parameter vector and $\xi_{\ell}(s; \boldsymbol{\theta})$ is the prediction based on the theoretical model presented in Section 3. The bin of the separation is the same as in the measurements but we introduce the minimum separation s_{\min} , i.e., excluding the data points at $s < s_{\min}$, to investigate the impact of small-scale information, which may suffer from less accuracy in the theoretical modelling. The inverse of the covariance matrix estimated by inverting the covariance matrix in Eq. (12) is not unbiased but can be corrected with Hartlap et al. (2007) factor:

$$\text{Cov}^{-1} \rightarrow \frac{N_{\text{BS}} - N_{\text{data}} - 2}{N_{\text{BS}} - 1} \text{Cov}^{-1}, \quad (15)$$

where N_{data} is the number of data points used in the analysis. Finally, the posterior distribution of parameters is explored with the Markov Chain Monte-Carlo (MCMC) method with *nautilus* sampler (Lange 2023). Flat priors are assumed for all three parameters. The live points are set to 10,000 and the sampling process runs until the effective sample size reaches 1,000.

In Figure 4, the posterior distribution of parameters by varying the minimum separation s_{\min} from $5 h^{-1}$ Mpc to $15 h^{-1}$ Mpc are shown for [O II] ELGs and control samples, respectively. As naively expected, increasing s_{\min} leads to broader constraints on parameters. Let us focus on the linear growth rate f , which is the only cosmological parameter in the analysis. For the control sample, the true value of f is recovered within the $1-\sigma$ level except for the case with $s_{\min} = 5 h^{-1}$ Mpc, where the theoretical model is no longer accurate enough due to the strong non-linearity. On the other hand, for [O II] ELGs, the inferred value of f is biased low with all choices of s_{\min} , consistent with the early study based on dark-matter-only simulations (Okumura & Jing 2011). This result indicates that the dynamics of ELGs within halos, which are not incorporated in the theoretical modelling, propagate as systematic mismodeling. The underestimation is qualitatively consistent with the dynamical nature of ELGs, i.e., ELGs are likely to undergo infall motion towards the halo centre, and thus, the velocity is lower than that of dark matter within halos. In other words, the assumption of no velocity bias ($\theta_g = \theta$) does not hold for ELGs.

The marginalised posterior distributions of parameters are shown in Figure 5. For [O II] ELGs, the linear growth rate f is finally recovered within a $1-\sigma$ level with $s_{\min} = 20 h^{-1}$ Mpc. The marginalized posterior distributions of the linear growth rate with $s_{\min} = 20 h^{-1}$ Mpc for the control sample indicates the bias over the $1-\sigma$ level. However, when the analysis is limited to large scales, the degeneracy between f and b_1 becomes severe, and thus, the bias apparently appears due to the projection effect. Figure 6 presents an example of the best-fitting multipole moments of anisotropic correlation functions with $s_{\min} = 10 h^{-1}$ Mpc for [O II] ELGs and control samples. The overall shapes of the best-fitting model are quite similar between [O II] ELGs and the control sample. The only difference is the amplitude of the quadrupole moment and that leads to a smaller inferred value of f for [O II] ELGs.

Similarly to the anisotropic correlation functions, we also perform the parameter inference with the isotropic correlation functions. In this case, the only free parameter is the linear bias b_1 . Hence, we do not run the MCMC sampling but directly compute the posterior distribution by evaluating the likelihood on a grid of b_1 . The results of the marginalised posterior distribution and the best-fitting isotropic correlation functions are shown in Figures 7 and 8, respectively. Both [O II] ELGs and the control sample yield similar constraints on b_1 except for the case with $r_{\min} = 20 h^{-1}$ Mpc, where the inferred value of b_1 is significantly lower compared with the isotropic case due to the degeneracy with f in the anisotropic analysis.

5 ELG-HALO CONNECTION

Next, we address the connection between ELGs and hosting halos to understand the origin of the systematic bias in the cosmological parameters inferred from the anisotropic correlation functions of ELGs.

The most widely used scheme to connect galaxies and halos is the HOD model and the HOD of simulated ELGs from IllustrisTNG has already been investigated in Paper I. Here, we summarise the main findings in that work. The HOD of ELGs significantly differs from that of LRGs, which are well described by the parametrised model proposed in Zheng et al. (2005). The ELG HOD exhibits the following features:

- The central HOD has a peak at the halo mass of $M_{\text{vir}} \sim 10^{12} h^{-1} M_{\odot}$, which corresponds to the infalling halos along filamentary structures. That feature can be captured by the HOD model tailored to ELGs (Geach et al. 2012).
- The large fraction of the halos around this peak mass scale are disk-dominated galaxies.
- The slope of satellite HOD is shallower than unity, which indicates quenching of star formation in massive halos.

Here, we extend the analysis to study the connection between ELGs and hosting halos, in particular for satellite ELGs.

5.1 Phase space distribution of satellites in hosting halos

To study the dynamics of satellite ELGs within halos, we measure the phase space distribution, i.e., the joint distribution of the radial position r and velocity v_r . Figure 9 presents the phase space distribution of satellite H α and [O II] ELGs. Here, the halo mass definition is the enclosed mass within the radius where the mean density is 200 times the critical density ρ_{cr} , which is denoted as M_{200c} . The radial position and velocity are normalised by the halo radius r_{200c} and the

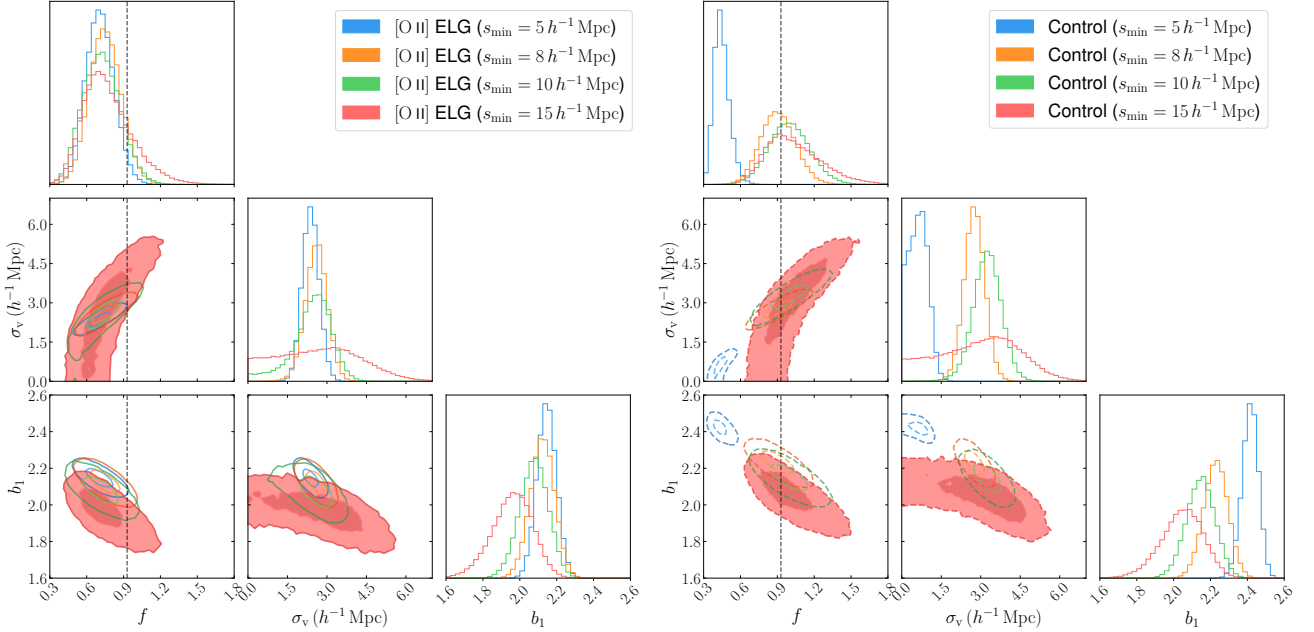


Figure 4. The parameter constraints with monopole and quadrupole moments of the anisotropic correlation function for [O II] ELGs (left panels) and the control sample (right panels). The contours correspond to 1- σ and 2- σ levels. The minimum separation s_{\min} is varied from $5 h^{-1} \text{ Mpc}$ to $15 h^{-1} \text{ Mpc}$.

circular velocity at the halo radius $v_{200c} = \sqrt{GM_{200c}/r_{200c}}$, respectively, where G is the gravitational constant. For the radial velocity, the sign is defined so that the positive (negative) value represents the outward (inward) motion relative to the halo centre. Both H α and [O II] ELGs exhibit two distinct components in the phase space: the virialised component ($\log(r/r_{200c}) \simeq -0.4$ and $v_r/v_{200c} \simeq 0$), and the infalling one ($\log(r/r_{200c}) \simeq 0.2$ and $v_r/v_{200c} \simeq -0.5$). If galaxies are completely virialised within halos, the 1D distribution of radial velocity is expected to be symmetric with a zero mean. To illustrate this, the distribution of dark matter particles in the same halos is overplotted as green dashed lines in Figure 9. There is a weak peak as the infalling component, but the dominant peak is the virialised component for dark matter. This feature indicates that satellite ELGs are preferentially located in the outskirts of halos rather than the virialised one and is consistent with the semi-analytic simulations (Orsi & Angulo 2018) and SHAM (Ortega-Martinez et al. 2025). It is widely assumed that the radial satellite distribution follows the Navarro–Frenk–White density profile (Navarro et al. 1996, 1997) but the deviation requires modifications to the approach to modelling clustering statistics based on HOD (see, e.g., Rocher et al. 2023).

The lifetime of line emission is $\sim 10 \text{ Myr}$ (Byler et al. 2018) and is much shorter than the dynamical time scale of halos t_{dyn} , which is given as

$$t_{\text{dyn}} = \frac{r_{200c}}{v_{200c}} = \sqrt{\frac{r_{200c}^3}{GM_{200c}}} = \left(\frac{4\pi}{3} G (200\rho_{\text{cr}}) \right)^{-\frac{1}{2}} = 616 \text{ Myr.} \quad (16)$$

Therefore, ELGs are likely to be recently accreted onto halos and quenched by the time they reach the pericentre. The observations (Blanton & Berlind 2007; Wetzel et al. 2012) also show that the quenched fraction of galaxies depends on the radius from the group or cluster centres.

Table 1. The fraction of ELGs and the mean halo mass with respect to the level of conformity. The halo mass definition is M_{200c} .

	Fraction (Number)	Mean halo mass ($h^{-1} M_{\odot}$)
H α ELG		
Central only	76.2% (4,673)	2.35×10^{12}
Satellite only	15.9% (975)	5.76×10^{12}
Conformal	7.9% (485)	1.24×10^{13}
[O II] ELG		
Central only	74.0% (6,985)	1.75×10^{12}
Satellite only	16.1% (1,517)	5.03×10^{12}
Conformal	9.9% (933)	9.60×10^{12}

5.2 Conformity

The galactic conformity refers to the correlation of properties of galaxies (Weinmann et al. 2006). Here, we address the conformity of the star formation activity in the ELG population. Table 1 presents the fraction of ELGs and the mean halo mass with respect to the level of conformity. The ratio is roughly consistent with the results based on semi-analytic or SHAM methods (see Figure 8 of Ortega-Martinez et al. 2025), though a different selection is adopted in that work. In terms of the mean halo mass, the halos hosting only central ELGs, only satellite ELGs, and both central and satellite ELGs (conformal halos) show the increasing trend in this order. The halos hosting only central ELGs are the dominant population among ELGs, and are likely to be independent halos. On the other hand, the conformal halos, here both central and satellite ELGs are found, are relatively massive halos. Halos hosting ELGs are infalling towards these massive halos, and the central galaxy undergoes star formation because the gas is still supplied to the galaxy in the dense core. Subhalos around this dense environment can also host ELGs and can be identified as satellite ELGs in the virialised component in the phase space distribution.

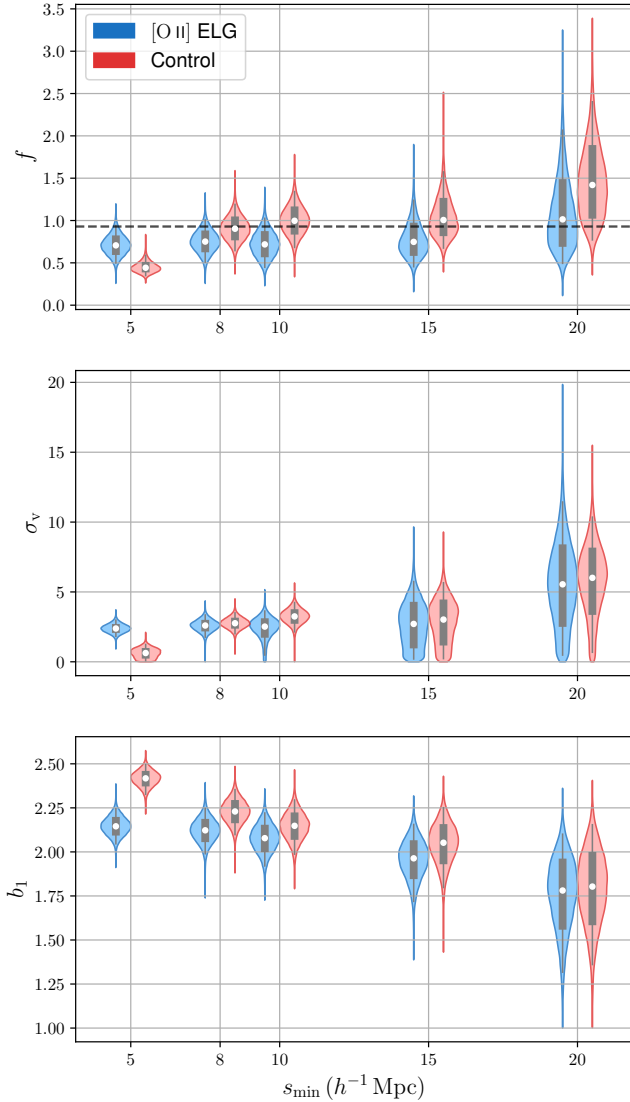


Figure 5. The marginalised posterior distributions with monopole and quadrupole moments of the anisotropic correlation function for [O II] ELGs and the control sample. The minimum separation s_{\min} is varied from $5 h^{-1}$ Mpc to $20 h^{-1}$ Mpc. The thick (thin) grey bars correspond to [15.87, 84.13] ([2.28, 97.72]) percentiles, and the white circles indicate the median values. The black dashed line corresponds to the true value of the linear growth rate f .

6 CONCLUSIONS

ELGs are the main target population of galaxies in the upcoming and ongoing Stage-IV spectroscopic surveys such as DESI, PFS, *Euclid*, and Roman Space Telescope. Previous works utilising semi-analytic models and hydrodynamical simulations have revealed that ELGs are likely to be located in the filaments or undergo infall towards massive halos. The dynamical nature specific to ELGs can have a significant impact on the clustering statistics in redshift space. The theoretical modelling of the clustering statistics has been proven to be accurate enough for LRGs. However, it is not clear whether the same modelling can be applied to ELGs without introducing any systematic bias in the inferred cosmological parameters.

In this work, we have performed the cosmology challenge with the

anisotropic correlation functions of ELGs using the realistic ELG catalogues (Paper I) constructed from the IllustrisTNG hydrodynamical simulations. In order to highlight the impact due to the dynamics of ELGs, we also construct the mass-limited control samples which have the same number density and a similar large-scale bias. Then, we have measured the anisotropic correlation functions of ELGs and performed the MCMC parameter inference with the theoretical model based on eTNS model at the 2-loop order. We have found that the inferred value of the linear growth rate f from monopole and quadrupole moments of anisotropic correlation functions of [O II] ELGs is biased low compared with the true value, though unbiased estimation is possible with the control sample. That underestimation can be attributed to the infalling motion of satellite ELGs towards the halo centre, which lowers the amplitude of the quadrupole moment. That is also an indication that the no velocity bias is not valid for ELGs.

In Paper I, it has been shown that the HOD of ELGs significantly differs from that of LRGs and the central ELGs are more likely to be disk-dominated isolated galaxies. To extend the analysis into the ELG-halo connection for satellite ELGs, we have investigated the phase space distribution of satellite ELGs within halos. A large fraction of satellite ELGs are found to be infalling towards the halo centre rather than virialised. This feature indicates that ELGs are likely to be recently accreted onto halos and quenched by the time they reach the pericentre. This feature justifies the hypothesis that ELGs have the specific dynamics within halos, which leads to the systematic bias in the inferred linear growth rate f . Next, we addressed the galactic conformity of star formation activity in ELG population. The conformity analysis has also supported this picture: the halos hosting both central and satellite ELGs are more massive than those hosting only central or satellite ELGs. 75% of halos hosting ELGs contain only central ELGs, 15% contain only satellite ELGs, and 10% contain both central and satellite ELGs. Most of halos hosting ELGs are central only ELG, and this is consistent with the fact that most of ELGs reside in the filamentary structures. The mean halo mass is the largest for the conformal halos, which can provide a dense environment to trigger star formation both in central and satellite galaxies.

In summary, we have demonstrated that the dynamics of ELGs within halos can lead to systematic bias in the cosmological parameters, in particular, the linear growth rate, inferred from the anisotropic correlation functions of ELGs at small scales. The accurate theoretical modelling taking into account the specific dynamics of ELGs is essential to fully exploit the cosmological information in the upcoming surveys. The analysis presented in this work provides useful insights into the small-scale clustering ELG. On the other hand, the large-scale clustering can also be probed by benefiting from the wide survey area in Stage-IV surveys. The large-scale clustering, especially BAO and AP effect, is not addressed in this work due to the limited box size of hydrodynamical simulations. Recently, the large-volume hydrodynamical simulations have become available (e.g., Hernández-Aguayo et al. 2023; Schaye et al. 2023). The impact at the large scales due to the specific dynamics of ELGs will be addressed in future work utilising those simulations.

ACKNOWLEDGEMENTS

This work was supported in part by JSPS KAKENHI Grant Number JP24H00215, JP25H01513, JP25K17380, JP22K21349, JP19KK0076 (K. O.). T. O. acknowledges support from the Taiwan National Science and Technology Council under Grants Nos.

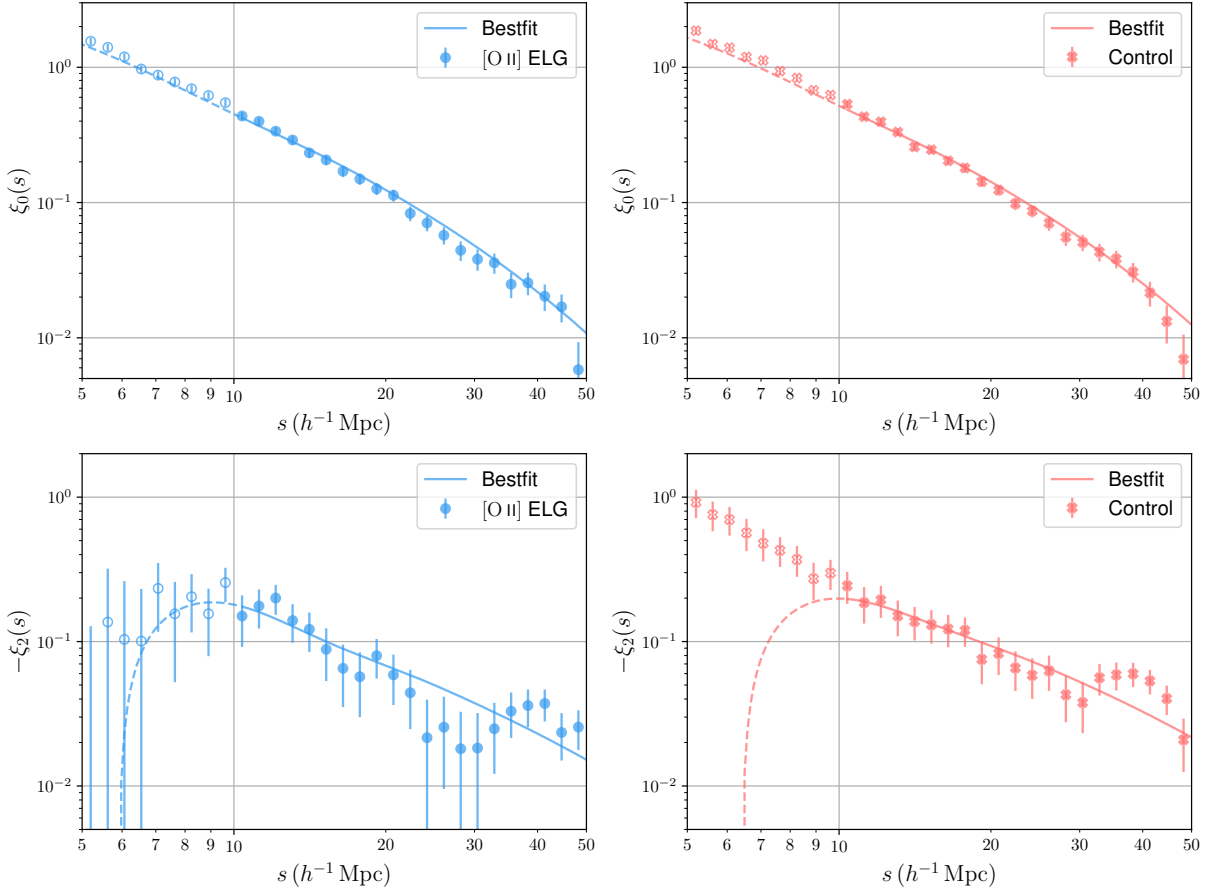


Figure 6. The best-fitting monopole and quadrupole moments of anisotropic correlation functions with $s_{\min} = 10 h^{-1} \text{ Mpc}$ for [O II] ELGs and the control sample. The dashed lines and unfilled symbols represent the predictions and the data points not used in the MCMC analysis, respectively.

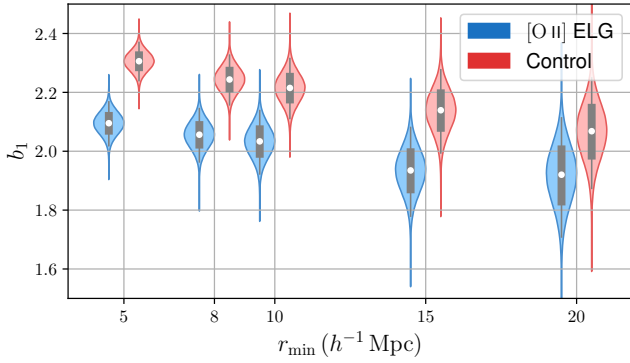


Figure 7. The marginalised posterior distributions with the isotropic correlation function for [O II] ELGs and the control sample. The minimum separation r_{\min} is varied from $5 h^{-1} \text{ Mpc}$ to $20 h^{-1} \text{ Mpc}$. The thick (thin) grey bars correspond to $[15.87, 84.13]$ ($[2.28, 97.72]$) percentiles, and the white circles indicate the median values.

NSTC 112-2112-M-001-034-, NSTC 113-2112-M-001-011- and NSTC 114-2112-M-001-004-, and the Academia Sinica Investigator Project Grant No. AS-IV-114-M03 for the period of 2025–2029. This work was supported in part by JGC-Saneyoshi Scholarship Foundation. The numerical calculations were carried out on Yukawa-21 at YITP in Kyoto University.

DATA AVAILABILITY

The catalogues of simulated ELGs are available upon reasonable request to the author.

REFERENCES

- Akeson R., et al., 2019, [arXiv e-prints](#), p. arXiv:1902.05569
- Alcock C., Paczynski B., 1979, *Nature*, **281**, 358
- Anderson L., et al., 2012, *MNRAS*, **427**, 3435
- Aubourg É., et al., 2015, *Phys. Rev. D*, **92**, 123516
- Avila S., et al., 2020, *MNRAS*, **499**, 5486
- Baldauf T., Seljak U., Desjacques V., McDonald P., 2012, *Phys. Rev. D*, **86**, 083540
- Barreira A., Lazeyras T., Schmidt F., 2021, *J. Cosmology Astropart. Phys.*, **2021**, 029
- Bel J., Pezzotta A., Carbone C., Sefusatti E., Guzzo L., 2019, *A&A*, **622**, A109
- Berlind A. A., Weinberg D. H., 2002, *ApJ*, **575**, 587
- Beutler F., et al., 2014, *MNRAS*, **443**, 1065
- Beutler F., et al., 2017, *MNRAS*, **466**, 2242
- Blanton M. R., Berlind A. A., 2007, *ApJ*, **664**, 791
- Byler N., Dalcanton J. J., Conroy C., Johnson B. D., Levesque E. M., Berg D. A., 2018, *ApJ*, **863**, 14
- Chan K. C., Scoccimarro R., Sheth R. K., 2012, *Phys. Rev. D*, **85**, 083509
- Charlot S., Fall S. M., 2000, *ApJ*, **539**, 718
- Charlot S., Longhetti M., 2001, *MNRAS*, **323**, 887
- Cole S., Lacey C. G., Baugh C. M., Frenk C. S., 2000, *MNRAS*, **319**, 168

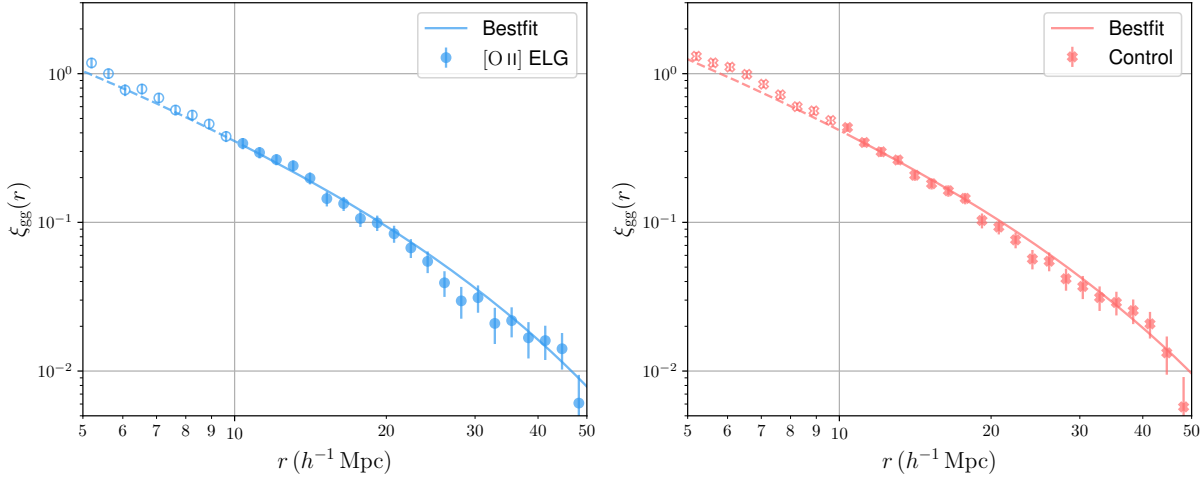


Figure 8. The best-fitting isotropic correlation functions with $r_{\min} = 10 h^{-1}$ Mpc for [O II] ELGs and the control sample. The dashed lines and unfilled symbols represent the predictions and the data points not used in the MCMC analysis, respectively.

DESI Collaboration 2022, *AJ*, **164**, 207
 DESI Collaboration 2024, *arXiv e-prints*, p. arXiv:2411.12021
 DESI Collaboration 2025a, *J. Cosmology Astropart. Phys.*, **2025**, 021
 DESI Collaboration 2025b, *J. Cosmology Astropart. Phys.*, **2025**, 012
 DESI Collaboration 2025c, *J. Cosmology Astropart. Phys.*, **2025**, 028
 Dawson K. S., et al., 2013, *AJ*, **145**, 10
 Eisenstein D. J., et al., 2001, *AJ*, **122**, 2267
 Eisenstein D. J., et al., 2005, *ApJ*, **633**, 560
 Euclid Collaboration 2025, *A&A*, **697**, A1
 Favole G., et al., 2020, *MNRAS*, **497**, 5432
 Favole G., Montero-Dorta A. D., Artale M. C., Contreras S., Zehavi I., Xu X., 2022, *MNRAS*, **509**, 1614
 Ferland G. J., et al., 2017, *Rev. Mex. Astron. Astrofis.*, **53**, 385
 Fioc M., Rocca-Volmerange B., 2019, *A&A*, **623**, A143
 Förster Schreiber N. M., Wuys S., 2020, *ARA&A*, **58**, 661
 Gao H., Jing Y. P., Zheng Y., Xu K., 2022, *ApJ*, **928**, 10
 Geach J. E., Smail I., Best P. N., Kurk J., Casali M., Ivison R. J., Coppin K., 2008, *MNRAS*, **388**, 1473
 Geach J. E., Sobral D., Hickox R. C., Wake D. A., Smail I., Best P. N., Baugh C. M., Stott J. P., 2012, *MNRAS*, **426**, 679
 Gil-Marín H., Noreña J., Verde L., Percival W. J., Wagner C., Manera M., Schneider D. P., 2015, *MNRAS*, **451**, 539
 Gonzalez-Perez V., et al., 2018, *MNRAS*, **474**, 4024
 Gonzalez-Perez V., et al., 2020, *MNRAS*, **498**, 1852
 Gutkin J., Charlton S., Bruzual G., 2016, *MNRAS*, **462**, 1757
 Hadzhiyska B., Tacchella S., Bose S., Eisenstein D. J., 2021, *MNRAS*, **502**, 359
 Hadzhiyska B., et al., 2023a, *MNRAS*, **524**, 2507
 Hadzhiyska B., et al., 2023b, *MNRAS*, **524**, 2524
 Hamilton A. J. S., 2000, *MNRAS*, **312**, 257
 Hartlap J., Simon P., Schneider P., 2007, *A&A*, **464**, 399
 Hayashi M., et al., 2018, *PASJ*, **70**, S17
 Hayashi M., et al., 2020, *PASJ*, **72**, 86
 Hearin A. P., Zentner A. R., van den Bosch F. C., Campbell D., Tollerud E., 2016, *MNRAS*, **460**, 2552
 Hernández-Aguayo C., et al., 2023, *MNRAS*, **524**, 2556
 Ishikawa S., Okumura T., Hayashi M., Takeuchi T. T., 2025, *MNRAS*, **539**, 2323
 Jackson J. C., 1972, *MNRAS*, **156**, 1P
 Kaiser N., 1987, *MNRAS*, **227**, 1
 Kewley L. J., Nicholls D. C., Sutherland R. S., 2019, *ARA&A*, **57**, 511
 Kravtsov A. V., Berlind A. A., Wechsler R. H., Klypin A. A., Gottlöber S., Allgood B., Primack J. R., 2004, *ApJ*, **609**, 35
 Lange J. U., 2023, *MNRAS*, **525**, 3181
 Lazeyras T., Wagner C., Baldauf T., Schmidt F., 2016, *J. Cosmology Astropart. Phys.*, **2016**, 018
 Madau P., Dickinson M., 2014, *ARA&A*, **52**, 415
 Marinacci F., et al., 2018, *MNRAS*, **480**, 5113
 McDonald P., Roy A., 2009, *J. Cosmology Astropart. Phys.*, **2009**, 020
 Mead A. J., Brienden S., Tröster T., Heymans C., 2021, *MNRAS*, **502**, 1401
 Mirbabayi M., Schmidt F., Zaldarriaga M., 2015, *J. Cosmology Astropart. Phys.*, **2015**, 030
 Naiman J. P., et al., 2018, *MNRAS*, **477**, 1206
 Navarro J. F., Frenk C. S., White S. D. M., 1996, *ApJ*, **462**, 563
 Navarro J. F., Frenk C. S., White S. D. M., 1997, *ApJ*, **490**, 493
 Nelson D., et al., 2018, *MNRAS*, **475**, 624
 Nelson D., et al., 2019, *Computational Astrophysics and Cosmology*, **6**, 2
 Norberg P., Baugh C. M., Gaztañaga E., Croton D. J., 2009, *MNRAS*, **396**, 19
 Okada H., et al., 2016, *PASJ*, **68**, 47
 Okumura T., Jing Y. P., 2011, *ApJ*, **726**, 5
 Okumura T., et al., 2016, *PASJ*, **68**, 38
 Okumura T., Hayashi M., Chiu I. N., Lin Y.-T., Osato K., Hsieh B.-C., Lin S.-C., 2021, *PASJ*, **73**, 1186
 Orsi Á. A., Angulo R. E., 2018, *MNRAS*, **475**, 2530
 Ortega-Martinez S., Contreras S., Angulo R., 2024, *A&A*, **689**, A66
 Ortega-Martinez S., Contreras S., Angulo R. E., Chaves-Montero J., 2025, *A&A*, **697**, A226
 Osato K., Okumura T., 2023, *MNRAS*, **519**, 1771
 Padmanabhan N., et al., 2007, *MNRAS*, **378**, 852
 Peebles P. J. E., Hauser M. G., 1974, *ApJS*, **28**, 19
 Pillepich A., et al., 2018a, *MNRAS*, **473**, 4077
 Pillepich A., et al., 2018b, *MNRAS*, **475**, 648
 Pu S.-Y., Okumura T., Chen C.-C., Nishimichi T., Akitsu K., 2025, *Phys. Rev. D*, **112**, L041302
 Raichoor A., et al., 2021, *MNRAS*, **500**, 3254
 Rapoport I., Desjacques V., Parimbelli G., Behar E., Crocce M., 2025, *ApJ*, **988**, 44
 Reid B., et al., 2016, *MNRAS*, **455**, 1553
 Rocher A., et al., 2023, *J. Cosmology Astropart. Phys.*, **2023**, 016
 Saito S., Baldauf T., Vlah Z., Seljak U., Okumura T., McDonald P., 2014, *Phys. Rev. D*, **90**, 123522
 Salim S., Narayanan D., 2020, *ARA&A*, **58**, 529
 Schaye J., et al., 2023, *MNRAS*, **526**, 4978
 Sheth R. K., Chan K. C., Scoccimarro R., 2013, *Phys. Rev. D*, **87**, 083002
 Sobral D., Best P. N., Matsuda Y., Smail I., Geach J. E., Cirasuolo M., 2012, *MNRAS*, **420**, 1926
 Spergel D., et al., 2015, *arXiv e-prints*, p. arXiv:1503.03757

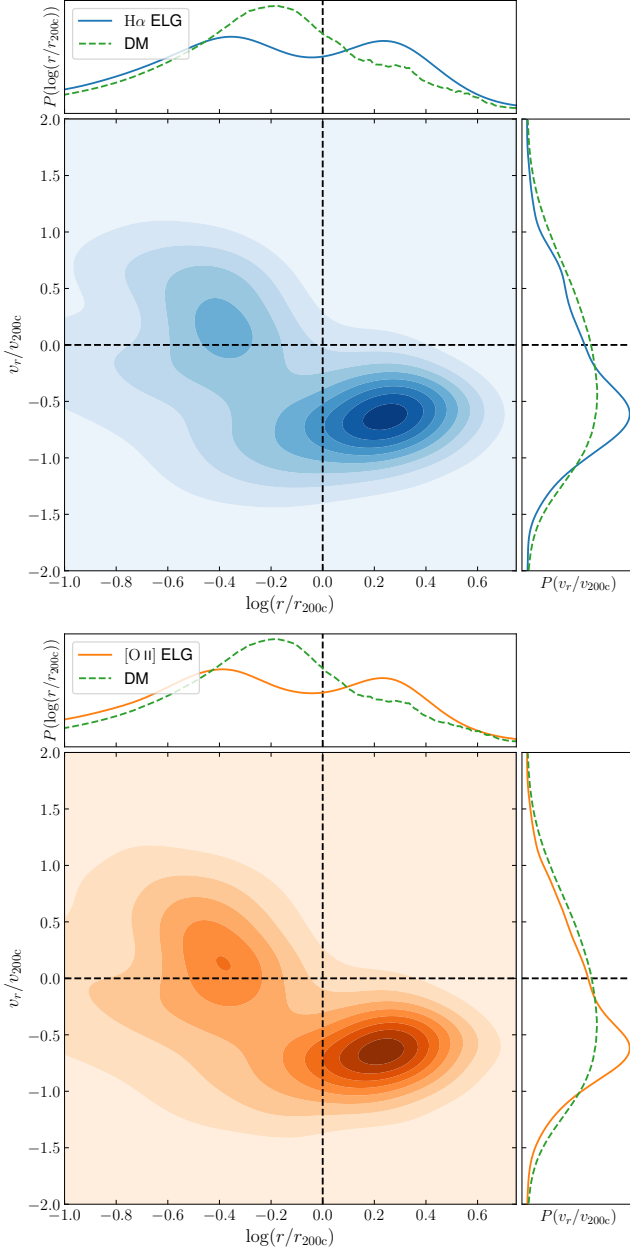


Figure 9. The phase space distribution of satellite H α and [OII] ELGs in hosting halos. The green dashed lines represent the distribution of dark matter (DM) particles in the same halos.

Springel V., 2010, *MNRAS*, **401**, 791
 Springel V., White S. D. M., Tormen G., Kauffmann G., 2001, *MNRAS*, **328**, 726
 Springel V., et al., 2018, *MNRAS*, **475**, 676
 Takada M., et al., 2014, *PASJ*, **66**, R1
 Tamone A., et al., 2020, *MNRAS*, **499**, 5527
 Taruya A., Nishimichi T., Saito S., 2010, *Phys. Rev. D*, **82**, 063522
 Taruya A., Bernardeau F., Nishimichi T., Codis S., 2012, *Phys. Rev. D*, **86**, 103528
 Taruya A., Nishimichi T., Bernardeau F., 2013, *Phys. Rev. D*, **87**, 083509
 Tonegawa M., et al., 2015, *PASJ*, **67**, 81
 Valageas P., Clerc N., 2012, *A&A*, **547**, A100
 Wechsler R. H., Tinker J. L., 2018, *ARA&A*, **56**, 435
 Weinberg D. H., Mortonson M. J., Eisenstein D. J., Hirata C., Riess A. G.,

Rozo E., 2013, *Phys. Rep.*, **530**, 87
 Weinberger R., et al., 2017, *MNRAS*, **465**, 3291
 Weinmann S. M., van den Bosch F. C., Yang X., Mo H. J., Croton D. J., Moore B., 2006, *MNRAS*, **372**, 1161
 Wetzel A. R., Tinker J. L., Conroy C., 2012, *MNRAS*, **424**, 232
 White S. D. M., Frenk C. S., 1991, *ApJ*, **379**, 52
 White S. D. M., Rees M. J., 1978, *MNRAS*, **183**, 341
 Yuan S., Hadzhiyska B., Bose S., Eisenstein D. J., 2022, *MNRAS*, **512**, 5793
 Yuan S., et al., 2025, *MNRAS*, **538**, 1216
 Zehavi I., et al., 2004, *ApJ*, **608**, 16
 Zheng Z., et al., 2005, *ApJ*, **633**, 791
 Zheng Z., Zehavi I., Eisenstein D. J., Weinberg D. H., Jing Y. P., 2009, *ApJ*, **707**, 554
 de Mattia A., et al., 2021, *MNRAS*, **501**, 5616

APPENDIX A: GALAXY POWER SPECTRA AT THE LEADING ORDER OF BIAS EXPANSION

Here, we describe the real-space galaxy spectra. Following McDonald & Roy (2009), we employ the galaxy power spectra with next-to-leading order bias terms:

$$P_{\delta_g \delta_g}(k) = b_1^2 P_{\delta \delta}(k) + 2b_1 b_2 P_{b2,\delta}(k) + 2b_{s2} b_1 P_{bs2,\delta}(k) + 2b_{3nl} b_1 \sigma_3^2(k) P_L(k) + b_2^2 P_{b22}(k) + 2b_2 b_{s2} P_{bs2}(k) + b_{s2}^2 P_{bs22}(k), \quad (A1)$$

$$P_{\delta_g \theta_g}(k) = b_1 P_{\delta \theta}(k) + b_2 P_{b2,\theta}(k) + b_{s2} P_{bs2,\theta}(k) + b_{3nl} \sigma_3^2(k) P_L(k), \quad (A2)$$

where δ is the density contrast of matter, and θ is the velocity divergence field of matter, $P_{\delta \delta}(k)$ and $P_{\delta \theta}(k)$ is the matter density-density auto-, and density-velocity cross-power spectra, respectively, and $P_L(k)$ is the linear matter power spectrum. By assuming no velocity bias, the velocity-velocity auto-power spectrum is given as

$$P_{\theta_g \theta_g}(k) = P_{\theta \theta}(k). \quad (A3)$$

The non-linear matter power spectrum $P_{\delta \delta}(k)$ is computed with **HMCODE-2020** (Mead et al. 2021). For the density-velocity and velocity-velocity power spectra, we adopt the fitting formulas in Bel et al. (2019):

$$P_{\theta \theta} = P_L(k) e^{-k(a_1 + a_2 k + a_3 k^2)}, \\ P_{\delta \theta} = [P_{\delta \delta}(k) P_L(k)]^{\frac{1}{2}} e^{-k/k_\delta - b k^6}, \quad (A4)$$

where the parameters are given as

$$a_1 = -0.817 + 3.198 \sigma_8(z), \quad (A5)$$

$$a_2 = 0.877 - 4.191 \sigma_8(z), \quad (A6)$$

$$a_3 = -1.199 + 4.629 \sigma_8(z), \quad (A7)$$

$$k_\delta / (h \text{ Mpc}^{-1}) = \left(-0.017 + 1.496 \sigma_8^2(z) \right)^{-1}, \quad (A8)$$

$$b = 0.091 + 0.702 \sigma_8^2(z), \quad (A9)$$

and $\sigma_8(z)$ is the amplitude of density fluctuation at the scale of $8 h^{-1}$ Mpc at the redshift z . The other bias terms are given as (Beutler

et al. 2014; Gil-Marín et al. 2015; Beutler et al. 2017):

$$P_{b2,\delta}(k) = \int \frac{d^3q}{(2\pi)^3} P_L(q) P_L(|\mathbf{k} - \mathbf{q}|) F_2(\mathbf{q}, \mathbf{k} - \mathbf{q}), \quad (A10)$$

$$P_{b2,\theta}(k) = \int \frac{d^3q}{(2\pi)^3} P_L(q) P_L(|\mathbf{k} - \mathbf{q}|) G_2(\mathbf{q}, \mathbf{k} - \mathbf{q}), \quad (A11)$$

$$P_{bs2,\delta}(k) = \int \frac{d^3q}{(2\pi)^3} P_L(q) P_L(|\mathbf{k} - \mathbf{q}|) \times F_2(\mathbf{q}, \mathbf{k} - \mathbf{q}) S_2(\mathbf{q}, \mathbf{k} - \mathbf{q}), \quad (A12)$$

$$P_{bs2,\theta}(k) = \int \frac{d^3q}{(2\pi)^3} P_L(q) P_L(|\mathbf{k} - \mathbf{q}|) \times G_2(\mathbf{q}, \mathbf{k} - \mathbf{q}) S_2(\mathbf{q}, \mathbf{k} - \mathbf{q}), \quad (A13)$$

$$P_{b22}(k) = \frac{1}{2} \int \frac{d^3q}{(2\pi)^3} P_L(q) [P_L(|\mathbf{k} - \mathbf{q}|) - P_L(q)], \quad (A14)$$

$$P_{b2s2}(k) = -\frac{1}{2} \int \frac{d^3q}{(2\pi)^3} P_L(q) \times \left[\frac{2}{3} P_L(q) - P_L(|\mathbf{k} - \mathbf{q}|) S_2(\mathbf{q}, \mathbf{k} - \mathbf{q}) \right], \quad (A15)$$

$$P_{bs22}(k) = -\frac{1}{2} \int \frac{d^3q}{(2\pi)^3} P_L(q) \times \left[\frac{4}{9} P_L(q) - P_L(|\mathbf{k} - \mathbf{q}|) S_2(\mathbf{q}, \mathbf{k} - \mathbf{q})^2 \right]. \quad (A16)$$

$$(A17)$$

$F_2(\mathbf{q}_1, \mathbf{q}_2)$, $G_2(\mathbf{q}_1, \mathbf{q}_2)$, and $S_2(\mathbf{q}_1, \mathbf{q}_2)$ are symmetrised second-order perturbation theory kernels:

$$F_2(\mathbf{q}_1, \mathbf{q}_2) = \frac{5}{7} + \frac{\mathbf{q}_1 \cdot \mathbf{q}_2}{2q_1 q_2} \left(\frac{q_1}{q_2} + \frac{q_2}{q_1} \right) + \frac{2}{7} \left(\frac{\mathbf{q}_1 \cdot \mathbf{q}_2}{q_1 q_2} \right)^2, \quad (A18)$$

$$G_2(\mathbf{q}_1, \mathbf{q}_2) = \frac{3}{7} + \frac{\mathbf{q}_1 \cdot \mathbf{q}_2}{2q_1 q_2} \left(\frac{q_1}{q_2} + \frac{q_2}{q_1} \right) + \frac{4}{7} \left(\frac{\mathbf{q}_1 \cdot \mathbf{q}_2}{q_1 q_2} \right)^2, \quad (A19)$$

$$S_2(\mathbf{q}_1, \mathbf{q}_2) = \left(\frac{\mathbf{q}_1 \cdot \mathbf{q}_2}{q_1 q_2} \right)^2 - \frac{1}{3}. \quad (A20)$$

$\sigma_3^2(k)$ is given as

$$\sigma_3^2(k) = \frac{105}{16} \int \frac{d^3q}{(2\pi)^3} P_L(q) \left[D_2(-\mathbf{q}, \mathbf{k}) S_2(\mathbf{q}, \mathbf{k} - \mathbf{q}) + \frac{8}{63} \right], \quad (A21)$$

where

$$D_2(\mathbf{q}_1, \mathbf{q}_2) = \frac{2}{7} \left[S_2(\mathbf{q}_1, \mathbf{q}_2) - \frac{2}{3} \right]. \quad (A22)$$

APPENDIX B: CONVERSION FUNCTIONS FOR MULTIPOLE EXPANSION

The dependence on the directional cosine μ in the eTNS 2-loop model except FoG damping the function is the polynomial at even degrees up to the octic, i.e., $D_{\text{FoG}}(k\mu\sigma_v)\mu^{2n}$ ($n = 0, 1, \dots, 4$). Thus, the integration in Eq. (7) can be done analytically. Here, we present the conversion formulae:

$$p_\ell^L(n, k) \equiv \frac{2\ell + 1}{2} \int_{-1}^{+1} \mu^{2n} \left(1 + \frac{\alpha\mu^2}{2} \right)^{-2} L_\ell(\mu) d\mu, \quad (B1)$$

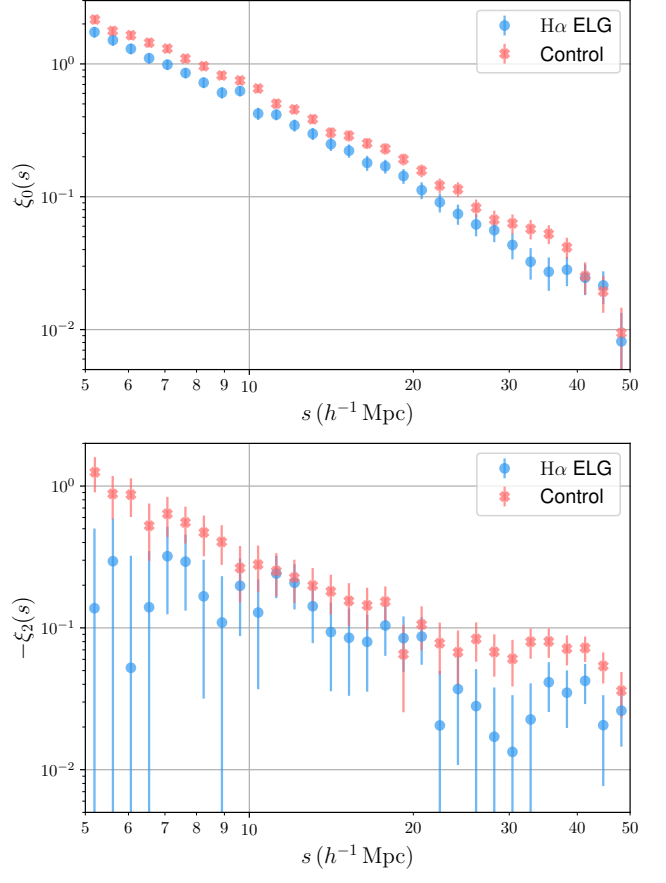


Figure C1. The multipole moments of correlation functions of H α ELGs and the corresponding control sample.

where $\alpha = (k\sigma_v)^2$. This function is analytically computed as

$$p_0^L(n, k) = \frac{1}{2} \left[-\frac{n - 1/2}{n + 1/2} {}_2F_1(1, n + 1/2; n + 3/2; -\alpha/2) + \frac{2}{\alpha + 2} \right] \quad (B2)$$

$$p_2^L(n, k) = \frac{5}{4} \left[\frac{n - 1/2}{n + 1/2} {}_2F_1(1, n + 1/2; n + 3/2; -\alpha/2) - 3 \frac{n + 1/2}{n + 3/2} {}_2F_1(1, n + 3/2; n + 5/2; -\alpha/2) + \frac{4}{\alpha + 2} \right], \quad (B3)$$

$$p_4^L(n, k) = \frac{9}{16} \left[-3 \frac{n - 1/2}{n + 1/2} {}_2F_1(1, n + 1/2; n + 3/2; -\alpha/2) + 30 \frac{n + 1/2}{n + 3/2} {}_2F_1(1, n + 3/2; n + 5/2; -\alpha/2) - 35 \frac{n + 3/2}{n + 5/2} {}_2F_1(1, n + 5/2; n + 7/2; -\alpha/2) + \frac{16}{\alpha + 2} \right], \quad (B4)$$

where ${}_2F_1(a, b, c; z)$ is the hypergeometric function.

APPENDIX C: SELECTED RESULTS FOR H α ELGS

Here, we present the results of the anisotropic correlation functions and the cosmological parameter inference for H α ELGs and the corresponding mass-limited control sample. The measurements of the

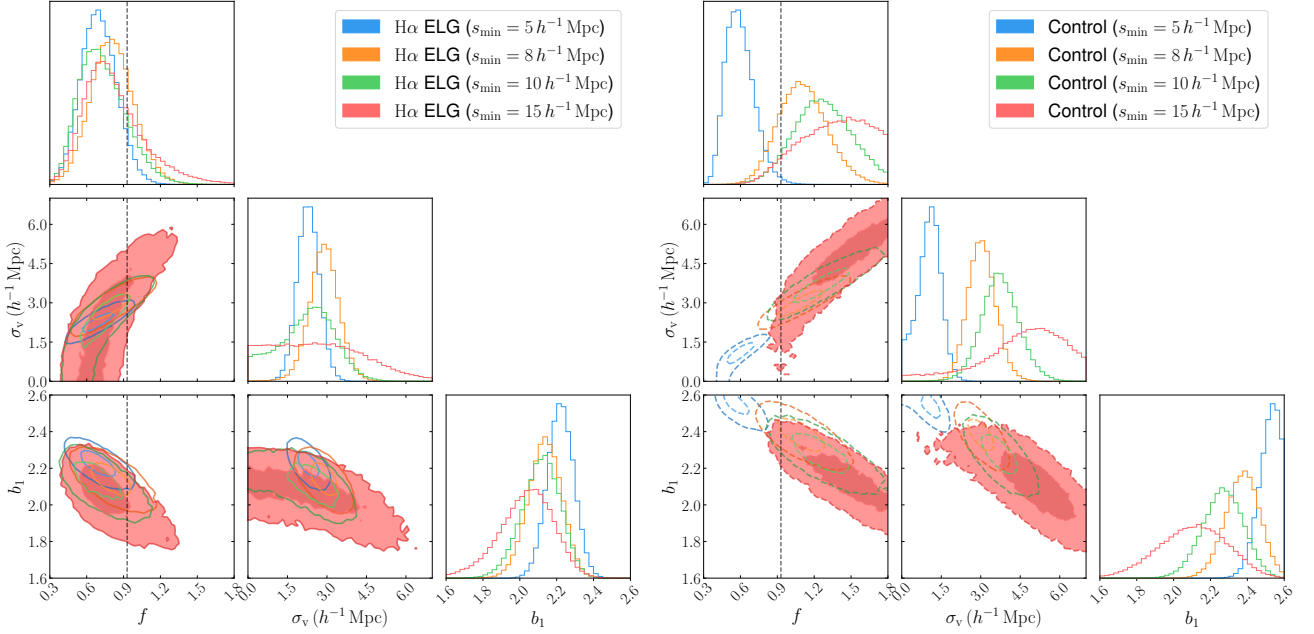


Figure C2. The parameter constraints with monopole and quadrupole moments of the anisotropic correlation function for H α ELGs (left panels) and the control sample (right panels). The contours correspond to 1- σ and 2- σ levels. The minimum separation s_{\min} is varied from $5\ h^{-1}\ \text{Mpc}$ to $15\ h^{-1}\ \text{Mpc}$.

multipole moments of anisotropic correlation functions are shown in Figure C1. The parameter inference results with varying the minimum separation s_{\min} are presented in Figures C2. The marginalised posterior distributions of parameters are shown in Figure C3. The qualitative features are similar to those of [O II] ELGs presented in Section 4. However, the H α ELG sample contains more galaxies than [O II] ELG sample, and thus, the control sample consists of less massive subhalos. For the control sample, the inferred linear growth rate is biased even for large s_{\max} due to the lower accuracy of modelling for such less massive subhalos. Nevertheless, comparing the inferred value between H α ELGs and the control sample, the values from H α ELGs are always smaller than that of the control sample, which indicate the velocity bias in H α ELGs as well as [O II] ELGs.

This paper has been typeset from a $\text{\TeX}/\text{\LaTeX}$ file prepared by the author.

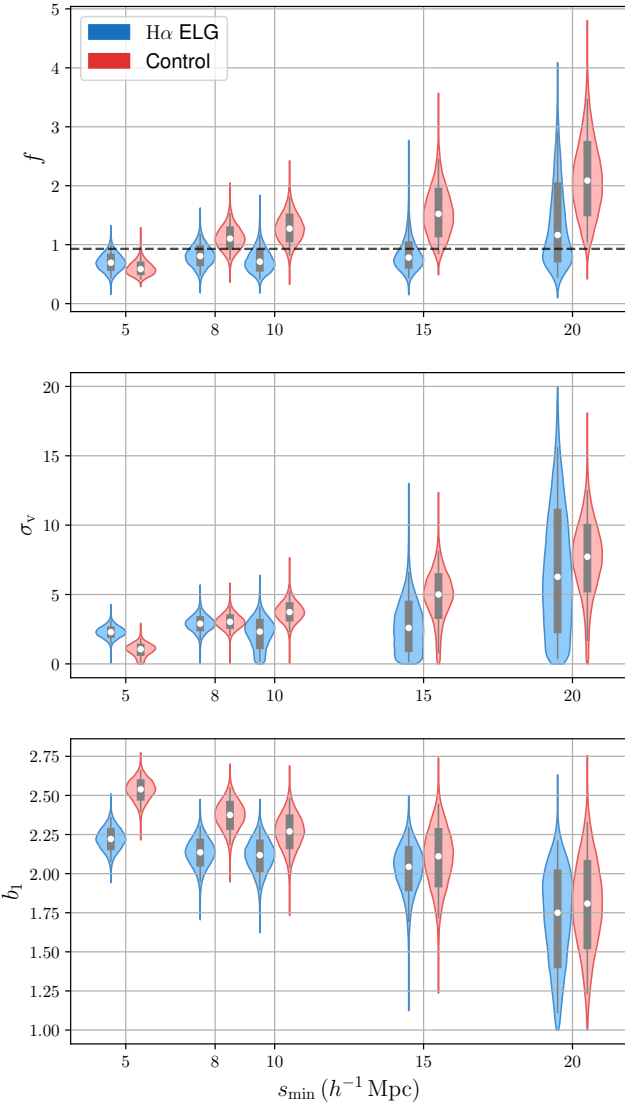


Figure C3. The marginalised posterior distributions with monopole and quadrupole moments of the anisotropic correlation function for [O II] ELGs and the control sample. The minimum separation s_{\min} is varied from $5 h^{-1}$ Mpc to $20 h^{-1}$ Mpc. The thick (thin) grey bars correspond to $[15.87, 84.13]$ ($[2.28, 97.72]$) percentiles, and the white circles indicate the median values. The black dashed line corresponds to the true value of the linear growth rate f .